

**Dislocations, texture and stress development in hydrogen-cycled Pd thin films
An in-situ X-ray diffraction study**

Verma, Neha; Delhez, Rob; van der Pers, N.M.; Hendrikx, R. W.A.; Huizenga, R. M.; Böttger, Amarante J.

DOI

[10.1016/j.ijhydene.2022.01.233](https://doi.org/10.1016/j.ijhydene.2022.01.233)

Publication date

2022

Document Version

Final published version

Published in

International Journal of Hydrogen Energy

Citation (APA)

Verma, N., Delhez, R., van der Pers, N. M., Hendrikx, R. W. A., Huizenga, R. M., & Böttger, A. J. (2022). Dislocations, texture and stress development in hydrogen-cycled Pd thin films: An in-situ X-ray diffraction study. *International Journal of Hydrogen Energy*, 47(24), 12119-12134. <https://doi.org/10.1016/j.ijhydene.2022.01.233>

Important note

To cite this publication, please use the final published version (if applicable).
Please check the document version above.

Copyright

Other than for strictly personal use, it is not permitted to download, forward or distribute the text or part of it, without the consent of the author(s) and/or copyright holder(s), unless the work is under an open content license such as Creative Commons.

Takedown policy

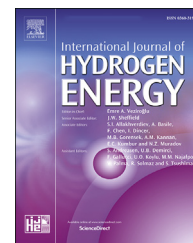
Please contact us and provide details if you believe this document breaches copyrights.
We will remove access to the work immediately and investigate your claim.



ELSEVIER

Available online at www.sciencedirect.com

ScienceDirect

journal homepage: www.elsevier.com/locate/ijhydene

Dislocations, texture and stress development in hydrogen-cycled Pd thin films: An in-situ X-ray diffraction study

Neha Verma^{*}, Rob Delhez, Niek M. van der Pers, R.W.A. Hendrikx, R.M. Huizenga, Amarante J. Böttger

Department of Materials Science and Engineering, Delft University of Technology, Mekelweg 2, 2628 CD Delft, the Netherlands

HIGHLIGHTS

- Pd thin films: microstructure and mechanical strength during hydrogen cycling studied.
- Cyclic deformation resulted in irreversible texture changes – sharpening of (111)-fiber texture.
- An open morphology restricts internal stress from amplifying during hydrogen uptake.
- All Pd films contain similar kinds of defects, that differ only by their concentration.
- The flexible PI inter-layer provides enhanced adhesive support, preventing strain localization and film delamination.

ARTICLE INFO

Article history:

Received 26 October 2021

Received in revised form

17 December 2021

Accepted 30 January 2022

Available online 24 February 2022

Keywords:

Pd thin films

XRD hydrogen cycling

Morphology

Texture

Stress

Dislocations

ABSTRACT

For Pd thin films, microstructural changes involved during hydrogen cycling provide the information needed to predict and optimize the film's mechanical strength. In this paper, a systematic study of the morphology, microstructure, texture, and stress has been performed on Pd thin films during hydrogen loading and deloading cycles at room temperature. Pd thin films of similar morphology were prepared by magnetron sputtering on substrates of different compliances, i.e., Si-oxide, Titanium (Ti) and Polyimide (PI). The evolution of the morphology, grain-orientation distribution (texture), state of stress, and dislocation densities are analyzed for each of the film substrate types for 20 hydrogen loading/deloading cycles. The lattice expansion and contraction caused by the transition from Pd to Pd-hydride and back result in a strong stress increase. This stress increase stabilizes after a few cycles by grain boundary motion that leads to a gradual enhancement of the (111) texture and changes in the dislocation density for Pd films that are strongly clamped on to an oxidized Si(100) wafer substrate with an intermediate layer (Ti or PI). For Pd on PI, the stress is also partly released by a crack-based (crack widening/growth/propagation) pathway. Pd films on Ti and PI do not buckle or blister after 20 hydrogen cycles. By providing a sufficiently compliant substrate the traditional problems of buckle-delamination of a film on a stiff substrate are mitigated.

© 2022 The Author(s). Published by Elsevier Ltd on behalf of Hydrogen Energy Publications LLC. This is an open access article under the CC BY-NC-ND license (<http://creativecommons.org/licenses/by-nc-nd/4.0/>).

^{*} Corresponding author. Department of Materials Science and Engineering, Delft University of Technology, Mekelweg 2, 2628 CD Delft, the Netherlands.

E-mail addresses: N.Verma@tudelft.nl, chem.neha@gmail.com (N. Verma), R.Delhez@tudelft.nl (R. Delhez), N.M.vanderPers@tudelft.nl (N.M. van der Pers), R.W.A.Hendrikx@tudelft.nl (R.W.A. Hendrikx), R.M.Huizenga@tudelft.nl (R.M. Huizenga), A.J.Bottger@tudelft.nl (A.J. Böttger).

<https://doi.org/10.1016/j.ijhydene.2022.01.233>

0360-3199/© 2022 The Author(s). Published by Elsevier Ltd on behalf of Hydrogen Energy Publications LLC. This is an open access article under the CC BY-NC-ND license (<http://creativecommons.org/licenses/by-nc-nd/4.0/>).

Introduction

For the successful development of a hydrogen (H) economy [1–3], the palladium-hydrogen (Pd-H) system has been extensively studied [4–7]. Palladium (Pd) and its alloys are often used in industry as a sensor [8,9], membrane [10,11], and storage [12,13] material for the detection, separation and purification of hydrogen. Pd interacts strongly with H and forms a solid solution hydride at room temperature [14]. Hydrogen readily dissociates on palladium surfaces. The hydrogen atoms adsorbed on the surface are in equilibrium with the absorbed subsurface hydrogen atoms that form palladium hydride within the metal lattice [15]. Nanostructuring of the metal hydrides provides a promising approach that has garnered substantial attention in the past decade [16,17]. Nanostructured Pd is reported to exhibit unique hydrogen absorption and desorption behavior [7], size-dependent hydriding thermodynamics and kinetics [18,19], as well as narrowing of the α -PdH_x and β -PdH_x miscibility gap [20,21]. Recent works have shown that the defective Pd nanoparticle has the ability to remove crystallographic imperfections, thereby enhancing the nano-sized system's durability under the stresses resulting from large volume changes during hydrogen absorption and desorption [22,23]. Hence, there is a lot of interest in studying the properties of Pd-based materials with significant potential for various energy-related applications.

In nanocrystalline (nc) thin films, phase boundaries and hydrogen solubility depend strongly on film growth morphology and microstructure (including texture and stress) [24,25]. The crystallographic orientation of the film depends on the deposition conditions as well as the substrate temperature [26]. Polycrystalline films can develop restricted crystallographic orientation distributions or textures during sputter deposition [27]. To estimate the orientation distribution of polycrystalline samples, it is often desirable to determine the volume fractions of different texture components. There are many methods to calculate these volume fractions, and the most commonly used is the orientation distribution function (ODF) [28]. For ODF analysis, at least three pole figures are required, thus leading to undesirably long data collection time. In addition, many ODF programs have difficulty handling weakly textured thin films. In the present study, texture is described in terms of simplified volume fraction analysis of the given components instead of an ODF or pole figure analysis. Since the studied Pd films have a fiber texture, the texture strength can be quantitatively represented from a single pole figure as a fiber texture plot (FTP).

For thin films, among various factors that affect hydrogenation [29,30], stress is employed to explain changes in film behavior as caused by elastic constraining from the underlying layer [31,32], which is known as substrate clamping. The presence of residual stress distributions can significantly impact the adhesion [31] and fracture toughness of thin films [33]. From experimental and fundamental points of view, intense research has been conducted for decades towards the reliable assessment of stress on a submicron scale [34]. In thin films, specific microstructure (texture, columnar grains, defects), film thickness, and grain size are responsible for the

macroscopic elastic anisotropy which influence diffraction-stress analysis [35]. In such a case, the so-called X-ray stress factors relate the lattice strain to mechanical stress and depend not only on the specific *HLK* reflections but also on the angles ψ and φ at which the strain was measured. Several grain interaction models have been proposed to study the elastic properties of thin films [36]; however, due to the actual geometric arrangement of grains, it is still quite difficult to take them into account. For thin films with fiber texture, one can use a technique that is similar to the one used for stress analysis in single crystals, the crystallite group method (CGM) [37]. This method was applied together with the conventional $\sin^2\psi$ method to estimate stress evolution in Pd thin film during hydrogen cycling.

The presence of stress in thin films leads to film cracking due to tensile stress, and buckling or blistering in the case of compressive stress. Global buckling and its driven delamination in thin films are typically observed on a stiff substrate [38]. The enormous field of fracture mechanisms has been developed to understand and predict the conditions under which cracks nucleate and propagate [39,40] so that cracking can be avoided in thin films. Lee et al. [41] utilize crack formation in Pd thin films, which, when exposed to hydrogen, expand laterally, altering the width of the cracks to produce reliable and reproducible multiple-cracked Pd film as a highly sensitive H₂ sensor. In the multiple-cracking phenomena, stresses are shared and transferred from one component to another, which prevents reaching a critical value of the strain energy. Thus, cracking could be used as a means to release H stress, but also a good adhesion between the thin film and the stiff substrate is required to avoid further film rupture by necking [42].

In the Pd-H system, the initial volume of the Pd structure expands by 10.4 vol% when the H/Pd ratio reaches about 0.5 [14]. This expansion can generate large compressive stresses if the deformation is deterred by a mechanical constraint imposed to a thin film lying on a thick substrate. Such fundamental issues have been addressed in our previous studies [43,44], where we used Pd thin films with open columnar morphology that stabilizes against embrittlement both at room temperature and at high temperature depending on the complexity of the intermediate layer used. We further investigate the stability of such Pd thin film systems after a long-term operation during hydrogen cycling in the current study. Flanagan et al. [45] have reported plastic deformation both during hydriding and dehydriding processes in Pd which leads to an overall increase of the dislocation density. Several transmission electron microscopy (TEM) studies have been dedicated to studying the dislocation-hydrogen interaction mechanisms and dislocation-mediated relaxation in hydride nc palladium films [30,46,47]. It is found that in nc materials grain boundaries act as rapid diffusion paths for hydrogen but also hydrogen diffusion is retarded due to hydrogen trapping by dislocations. More generally, because of the complexity of the microstructure of nc metals, the microstructural changes associated with the phase transformations strongly differ from coarse-grained metals.

In this work, three different Pd thin films, sputter-deposited with and without intermediate layer but with practically identical microstructures, were studied. This allowed us to

deduce the influence of the intermediate layer (substrate types) on the morphology, preferred orientation (texture), state of stress and dislocation density as a function of hydrogen cycling. It was found that the cyclic process results in an irreversible texture change. The stress analysis results show that the stress evolution during cycling is different for all three Pd thin film systems, and the film-substrate interface determines the deformation behavior. These findings are further supported by transmission and scanning electron microscopy (TEM and SEM) investigations for morphological changes. XRD line-broadening analysis was used to investigate the (plastic) deformation mechanism.

Experimental

Pd thin film preparation

The Pd thin films of 100 ± 10 nm thickness were dc-magnetron sputter deposited. The process details are described in our previous work [44]. In brief, Pd was deposited for 900 s in an argon (Ar) atmosphere at 3 Pa. The gun (Pd target with 99.95% purity) was operated at 100 W dc power with an average deposition rate of 0.1 nm/s. The Pd thin films were deposited at room temperature onto three different substrate types: (i) thermally oxidized (~ 188 nm) single-crystal Si(100) wafer (SiO₂/Si), (ii) a sputter-deposited Titanium (Ti) interlayer on a SiO₂/Si wafer (Ti-SiO₂/Si) and (iii) a spin-coated polyimide (PI) interlayer on a SiO₂/Si wafer (PI-SiO₂/Si). About 6 nm Ti interlayer was deposited during 360 s at 3 Pa Ar pressure (0.016 nm/s) [43]. The PI (5 μ m) spin-coated SiO₂/Si wafers were prepared at Else Kooi Lab (EKL), TU Delft. After deposition, the Pd thin films were transferred into a single wafer container and stored at room temperature.

Investigation of cross-sectional morphology of Pd thin film was performed using CM30T and CM300UT-FEG Philips Transmission Electron Microscopy (TEM), type Tecnai F20ST/STEM (FEI Electron Microscopes) with energy dispersive spectroscopy (EDS). Scanning electron microscopy (SEM) JEOL JSM 6500F from Japan Electron Optics Ltd was used to investigate the changes related to the surface morphology of Pd thin film (e.g., microcracks and blisters) upon hydrogen loading/deloading.

X-ray diffraction (XRD)

In view of the availability and comparability of data from two different diffractometer settings, the hydrogen cycling experiments were performed in focusing geometry (Bruker-AXS D5005) and parallel-beam geometry (Bruker-AXS D8).

Focusing optics diffractometer: hydrogen cycling

20 slow hydrogen loading/deloading cycles (20-L/D) were performed on an *in-situ* XRD set-up: Bruker-AXS D5005 diffractometer in a Bragg-Brentano focusing geometry (CuK α ; 45 kV, 30 mA), equipped with an MRI HT chamber (D5005). The chamber is supplied with a mass flow controller to conduct loading in 5%H₂ + 95%N₂ (pH₂) = 0.05 atm gas mixture and deloading in N₂ (1 atm) gas. The measurements were performed at room temperature and atmospheric pressure.

The *in-situ* set-up was used to monitor hydrogen cycling and measure stress developed during hydrogen loading/deloading in Pd films simultaneously. For slow 20-L/D cycles, continuous 2 min short scans (Supplementary Fig. S1) in the range 36–43° 2 θ (including peaks of the Pd- α and β phases) were made until complete loading and deloading had been achieved at each cycle. This was followed by a long overview scan (Supplementary Fig. S2) over three ranges: 36–43° 2 θ (including the Pd-{111}), 43–50° 2 θ (including the Pd-{200}) and 74–90° 2 θ (including the Pd- {311} and {222} reflections) for the numerical evaluation of microstructural changes. For each range, counting time and step size were chosen to take into consideration the counting statistics of the weaker diffraction peaks. The instrumental profile was determined by measuring, under analogous conditions, NIST/NBS LaB6 powder (SRM660a) [48] on a Si(510) single-crystal substrate.

In between cycling, in-plane stress was measured after the 1st, 5th, 10th, 15th, and 20th L/D cycles by applying instrumental omega-tilt (tube: $\theta + \omega$; detector: $\theta - \omega$) using the Pd- α and Pd- β {331} and {420} reflections (Supplementary Fig. S3). Omega-offset was provided for ψ -tilt angles 0°–45° in step mode ($\sin^2\psi \approx 0$ –0.5 in steps of 0.1). Pd- α at $\sin^2\psi \approx 0.2$ and 0.3 and Pd- β at $\sin^2\psi \approx 0.3$ and 0.4 of {331} and {420} reflections were not used because at these omega-tilt angles, the window frame of the MRI chamber obstructs the diffraction signal. Therefore, only four points were used for the lattice strain measurement (Supplementary Fig. S13(b) & 14(b)). The total measurement times for omega-stress scans ranged from 22 to 24 hours. The counting time was rather long on purpose to detect minimal variations due to counting statistics. Since the D5005 system has focusing optics, defocusing errors due to omega-tilting are inevitable. For defocusing correction, Palladium powder (AlFa-D24F20) was used for which the stress-free state has been checked with the $\sin^2\psi$ method using a parallel-beam diffractometer.

Parallel-beam diffractometer: hydrogen cycling

In contrast to the D5005 system, the parallel-beam geometry allows measurements at large tilt angles without defocusing, whereas also specimen position and roughness are not critical. However, primarily the hydrogen cycling experiments were repeated on this diffractometer to provide a way to simultaneously monitor texture and stress in Pd thin films during hydrogen cycling.

In this *in-situ* XRD set-up (Supplementary Fig. S4), a Pd thin film for 20-L/D cycles was mounted (using vacuum grease) in the custom-made specimen holder connected to a Bruker D8 diffractometer in parallel-beam optics equipped with Huber ¼ Eulerian cradle, called the PSI-XRD system. The holder consists of a cavity covered by a transparent foil Chemplex Pro-lene® of 4 μ m thickness, enabling direct visualization of the topographic changes in Pd thin film upon hydriding. CoK α radiation ($\lambda = 0.179026$ nm) appears from the point focus geometry of the sealed X-ray tube operated at 45 kV and 25 mA. The diffracted beam passed a parallel soller slit of 0.35° and a graphite monochromator before reaching the detector.

For each loading and deloading cycle, the transformation was monitored by a loop of short scans in the 2 θ range 43–49° (Supplementary Fig. S5&6), containing the Pd-{111} reflections of the α - and β -phase. Using a step size of 0.05° 2 θ and a

counting time per step of 1 s, the time per scan is 2 min. The loop scans enabled to follow the start and finish of each transformation in time and detail. In order to monitor change in line-width, overview long scan in the 2θ range $40\text{--}110^\circ$ (Supplementary Fig. S7), including the Pd- {111}, {200}, {311} and {222} reflections was made with an omega offset of 2° to avoid the very strong Si{400} from the substrate. Under ambient conditions, hydrogen loading was conducted in a gas mixture of $5\%H_2 + 95\%N_2$ ($p_{H_2} = 0.05$ atm) and deloading in N_2 gas (1 atm). The scanning sequence included: (1) loading short loop scans, (2) loading long overview scan, (3) texture/stress measurements under loading condition, (4) deloading short loop scans, (5) deloading long overview scan, and (6) texture/stress measurements under deloading condition. This sequence was repeated for each cycle, except that texture/stress measurements were performed only for cycle 1, 5, 10, 15, and 20. The data evaluation of the diffraction profiles was done with the program Bruker – EVA [49].

Texture and stress measurements

When high stresses are present, a conventional method based on pole figures cannot be used for texture determination since the 2θ peak position considerably changes with ψ -tilting [50]. In this work, after ensuring the fiber symmetry of the crystallographic texture (Supplementary Fig. S8), the measurement strategy of collecting the entire diffraction peak (θ - 2θ scan) for different sample ψ -tilt angles at fixed rotation angle φ was adopted. The rotation direction was chosen such that no disturbance occurred by the diffraction from the single-crystalline Si wafer. The intensities of the diffraction lines Pd- {111}, {200} and {311} were recorded as a function of ψ -tilt angle (Supplementary Fig. S9). The ψ range is $0^\circ\text{--}75^\circ$ in steps of 10° and total scan time 30 hours. The incident beam size is adjusted with a crossed slits assembly which enables to limit the beam in two perpendicular directions: height and width. Sample size and incident beam size combination were carefully chosen, such that the irradiated area did not exceed the specimen surface area at all orientations of the samples [51]. The characteristic parameters of the individual peaks were evaluated by fitting pseudo-Voigt functions to the measured data using the software package PANalytical X'Pert Stress Plus [52]. Additional data processing was applied as required for texture and stress analysis.

XRD line-broadening: microstructure characterization

The deformation in terms of defect parameters such as crystallite sizes and dislocations densities were obtained by line-broadening analysis of X-ray diffraction profiles using the integral breadth [53]. The analysis was performed on long overview scans (Supplementary Fig. S2). from 20 hydrogen loading/deloading cycles run on the Bruker D5005 set-up (Section Focusing optics diffractometer: Hydrogen cycling). The measurement and data analysis details are described in our previous work [44].

The measured XRD peak profile and broadening is the result of the convolution of the instrumental broadening of the diffractometer and the broadening introduced by microstructural imperfections in the sample called microstructural broadening. The instrument-corrected broadening

β_{hkl} corresponding to the diffracted peak of Pd thin film was estimated using:

$$\beta_{hkl} = \left[(\beta_{hkl})_{\text{measured}}^2 - (\beta_{hkl})_{\text{instrumental}}^2 \right]^{1/2} \quad (1)$$

because the shape of all line profiles involved was close to Gaussian as found from profile fitting.

In the rest of this study β_{hkl}^* , the integral breadth in reciprocal space is used instead of β_{hkl} :

$$\beta_{hkl}^* = \beta_{hkl} \cos \theta / \lambda \quad (2)$$

It is assumed here that the microstructural broadening was caused by crystal imperfections and small crystallite size, and that the effects of broadening by crystallite size and by crystal imperfections are additive.

The more probable crystal imperfections appear to be dislocations. We concluded, based on the lattice constants obtained from the measured line profiles, that stacking and twin faults are very unlikely to significantly contribute to the line broadening [54]. Therefore the line breadths were evaluated by the modified Williamson-Hall (mod-WH) method [55,56]. The method accounts for the anisotropic strain fields of dislocations by introducing the Contrast Factor C_{hkl} of dislocations. C_{hkl} depends on the types, densities, and arrangements of the dislocations present, as well as on the orientation distribution of the dislocations with respect to the diffraction vector g_{hkl} . The integral breadth is given by

$$\beta_{hkl}^* = K \left\langle D \right\rangle + \left(\pi M^2 b^2 / 2 \right)^{1/2} \left[(h^2 + k^2 + l^2) / a^2 \right]^{1/2} \rho^{1/2} C_{hkl}^{1/2} \quad (3)$$

where K is a constant (here taken as 1), $\langle D \rangle$ (nm) is the average crystallite size (perpendicular to the Pd layers), M is a constant describing the dislocation arrangement [57] (here taken as 1), ρ is the dislocation density (m^{-2}), b is the length of the Burgers vector, and a is the lattice constant. The calculated contrast factors for Pd thin films are provided in our previous work [44].

Results and discussion

Morphology analysis: evolution during cycling

To divulge the influence of the intermediate layer (substrate type) on hydrogen cycling, we envisioned growing comparable Pd films with open morphology (and texture) on all substrates. In our previous works [43,44,58], it was shown that a Pd thin film with an open columnar structure is stabilized against embrittlement. Fig. 1 shows TEM bright-field images of Pd thin films with an adhesive intermediate layer (Pd on Ti and Pd on PI) in an as-deposited state and after 20 hydrogen loading/deloading cycles (20-L/D). One clear feature in all Pd thin film specimens is the presence of elongated voids at part of the grain boundaries (Fig. 1(a–d)). Columnar structures are more or less elongated in shape, and some columns run (almost) from top to bottom. The observed Pd thin-film features like grain size, voids, and twins showed no major difference between the four investigated film specimens (Table 1). TEM could not be

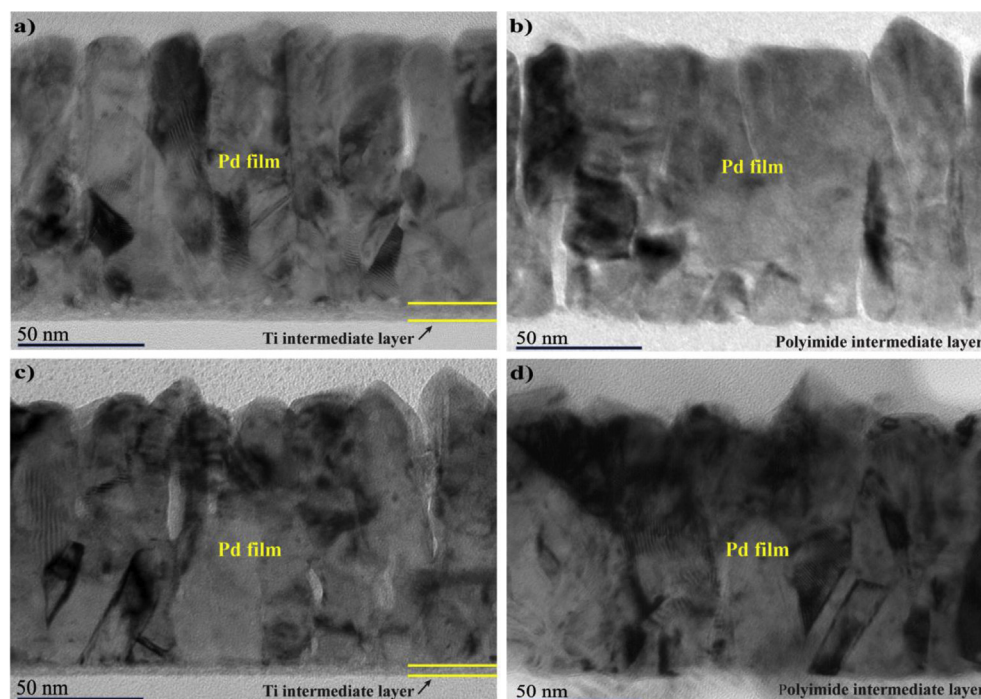


Fig. 1 – A cross-sectional view of TEM bright-field (BF) images of ~100 nm Pd thin films. Film morphology in as-deposited state: (a) Pd-Ti-SiO₂/Si and (b) Pd-PI-SiO₂/Si, and after 20 hydrogen loading/deloading cycles (20-L/D): (c) Pd-Ti-SiO₂/Si and (d) Pd-PI-SiO₂/Si. All Pd film specimens show open columnar structures which are more or less elongated in shape, often running from top to bottom.

Table 1 – TEM investigated microstructural features indicated for Pd-Ti-SiO₂/Si and Pd-PI-SiO₂/Si films in as-deposited state and after 20 hydrogen loading/deloading cycles (20-L/D).

	Pd Thickness (nm)	Ti Thickness (nm)	Grain size (nm) (width x height)	Twins	Voids (nm) (width x height)
Pd-Ti-SiO ₂ /Si (as-dept.)	110–125	7.5 ± 0.7	15 × 15–20 × 80	yes	>3 × 90
Pd-PI-SiO ₂ /Si (as-dept.)	110–140	–	(20–50) × (20–120)	yes	(2–6) × (20–50)
Pd-Ti-SiO ₂ /Si (after 20-L/D)	100–120	3 ± 0.5	(15–25) × (80–100)	yes	(2–7) × (7–25)
Pd-PI-SiO ₂ /Si (after 20-L/D)	105–135	–	6 × 20–25 × 75	yes	(2–3) × (20–60)

performed on Pd film without intermediate layer (Pd-SiO₂/Si, Pd-Ti-SiO₂/Si, and Pd-PI-SiO₂/Si) due to Pd layer buckle-delamination after 20-L/D cycles; contrarily, Pd-Ti-SiO₂/Si and Pd-PI-SiO₂/Si films remained strongly adhered to the substrate. TEM images of as-deposited Pd thin films with and without intermediate layer are also shown in our previous work [44].

Fig. 2 shows the SEM planar view of as-deposited Pd films in the first row and Pd films at the end of 20-L/D cycles in the second row. Fig. 2(a–c) at 10 μm scale have a smooth appearance in the as-deposited condition, and high magnification (100 nm) insets show low-density open morphology for all Pd films with and without intermediate layers. Exposure to hydrogen causes the Pd film to expand, and upon subsequent deloading, it returns to its original state [20]. During hydrogen loading films are subjected to biaxial compressive stress due to which the film buckles, thus releasing most of the stress [32]. However, the real-time monitoring of cycling experiments on the PSI-XRD system showed the absence of buckle formation during hydrogen loading for all Pd films studied. In other words, the open

columnar structures allow Pd thin film clamped on a stiff substrate to breathe (expand) during hydrogen uptake. In contrast, Pd films with close columnar structures had shown buckle formation during loading and buckle-delamination after the α ↔ β phase transformation [44].

SEM micrographs in Fig. 3 compare surface topography of Pd-SiO₂/Si film after 1, 5, 10, 15 and 20-L/D cycles with respect to its as-deposited state. Already after the first hydrogen cycle, Fig. 3(b), Pd film shows widening of existing as-deposited microcracks. Microcrack initiation starts at a surface defect because of the highly localized strain concentration at the grain boundaries [59]. Further cycling increases microcrack width gradually, as seen in subsequent SEM images Fig. 3(c–f). In the beginning, microcracks form a fine web network (Fig. 3(b) inset), but with cycling, scattered wide cracks occur, as seen in Fig. 3(c–f) inset. In the evolving film morphology after cycling, islands of compact morphology between wide cracks are found. The microcrack propagation is followed by buckling. Complementary optical microscopy (OM) images in Fig. 4(a) show buckled morphology on the film surface

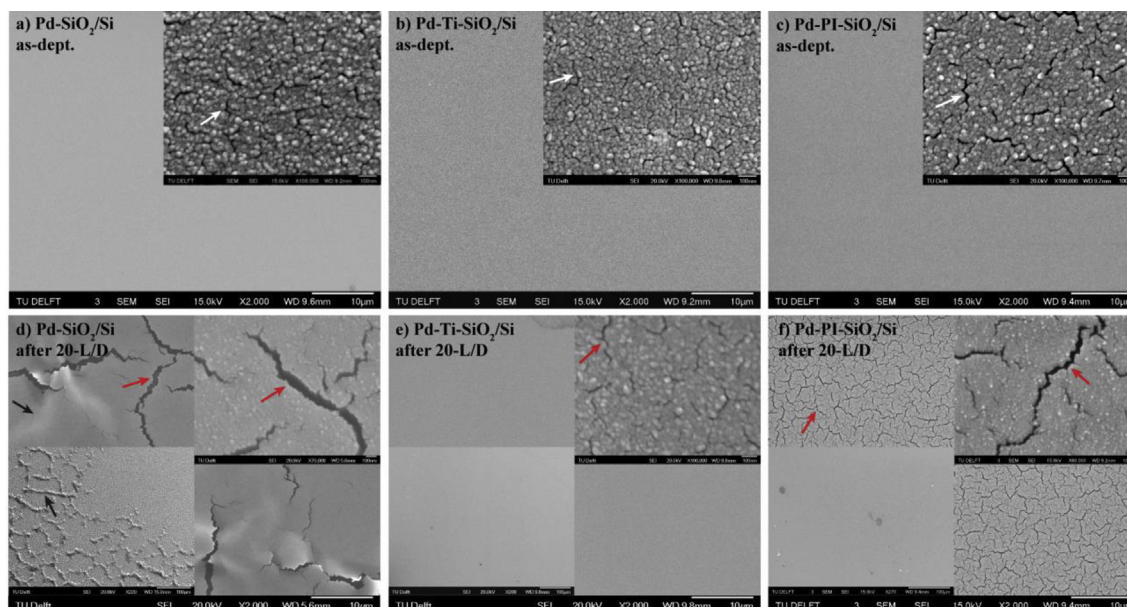


Fig. 2 – SEM images illustrating surface morphology of as-deposited and hydrogen cycled Pd thin films. From left to right: a&d) Pd-SiO₂/Si, b&e) Pd-Ti-SiO₂/Si and c&f) Pd-Pt-SiO₂/Si. The top layer contains as-deposited films with large images at a 10 μm scale and the inset images at a 100 nm scale. The bottom layer includes films after 20 hydrogen loading/deloading cycles (20-L/D) with large images of 10 μm scale and the inset images at 100 nm and 100 μm scales. The white arrows indicate as-deposited networks of primary microcracks associated with intercolumnar voids. The red arrows indicate hydrogen-induced microcracks, and the black arrows indicate delamination buckles or blisters in Pd-SiO₂/Si film after 20-L/D cycles. Note that the micrographs of as-deposited films and films after 20-L/D are from two different samples. (For interpretation of the references to colour in this figure legend, the reader is referred to the Web version of this article.)

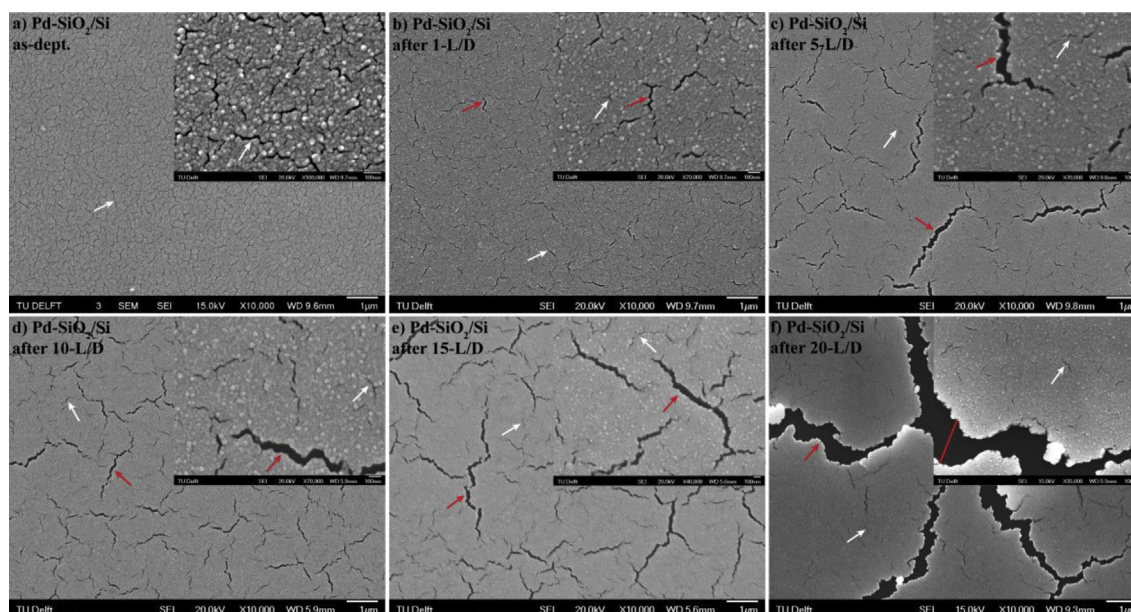


Fig. 3 – SEM micrographs with low (10 μm) and high magnification (100 nm) illustrates surface morphology of a Pd-SiO₂/Si thin film in different states: (a) as-deposited, (b), (c), (d), (e), and (f) corresponds to the loading/deloading cycle numbers of 1, 5, 10, 15 and 20, respectively. The white arrows indicate as-deposited distributed microcracks and the red arrows indicate a hydrogen-induced widening of microcracks after loading/deloading cycle/cycles. Note that the micrographs were taken from six different samples. (For interpretation of the references to colour in this figure legend, the reader is referred to the Web version of this article.)

observed only after exposure to 10-L/D cycles. The onset of buckling starts from the specimen edge, propagating towards the center. Strain localization facilitates microcrack propagation through the buckled region, which provides the additional driving force for the film delamination. Consequently, after 20-L/D hydrogen cycles, the Pd film on bare SiO₂/Si substrate exhibits peel-off traces of buckles with wide microcracks and wrinkles all over the film specimen (Figs. 2(d), 3(f) and 4(c)). Delaminated margins are seen as bright areas around the microcracks in SEM images. Here, due to weak cohesion between the Pd film and the substrate, the structural integrity of the thin-film system is compromised to facilitate stress relaxation.

Microcrack propagation (growth and widening) during hydrogen cycling is limited for the Pd-Ti-SiO₂/Si film. After 20-L/D cycles, the film structure remained very similar to the as-deposited state (Fig. 2(e)) with very few scattered and rather narrow microcracks visible only in high-magnification (100 nm scale), top inset of Fig. 2(e). The surface morphological results demonstrate that a Ti adhesive intermediate layer substantially improves the Pd film compliance – the stability of the film during hydrogen cycling. For sputtered metal films of columnar morphology, intergranular spacing along grain boundaries can increase compliance [60]. Such morphology allows smooth phase transitions in the Pd-Ti-SiO₂/Si film, where the Pd film cannot be stretched due to reinforced film adhesion to the rigid substrate. The open morphology of the Pd film and the strong interface bonding between the film and underlying substrate facilitate each other, resulting in a stable Pd thin film system. However, the rigid substrate confines the deformation of the film in its plane. To rationalize these observations, further XRD microstructural analysis is conducted and reported in the following sections.

Similarly, Pd-PI-SiO₂/Si film endures strain accumulation and relaxation during 20-L/D cycles. As opposed to a blister-delaminated surface that is visible at 100 μm scale for Pd film without intermediate layer (Fig. 2(d) bottom inset), Pd on PI film appears smooth at the same magnification (Fig. 2(f) bottom inset). Hydrogen-cycling induced microcracks are uniformly spread in the large image of 10 μm scale (Fig. 2(f)) contrary to a smooth surface in the as-deposited condition in Fig. 2(c). In the high magnification top inset of Fig. 2(f), we see a few as-deposited primary microcracks and more compact morphology as compared to open as-deposited morphology in

the inset of Fig. 2(c). PI intermediate layer plays a pivotal role in providing a flexible alternative to elasticity limitation inherent to the thin film supported on a stiff substrate [42]. The enhancement of film-substrate adhesion can suppress strain localization [33,61], allowing for a homogenous deformation, such that Pd film can recover from high total strain due to lattice expansion. An increase in microcrack spacing was noticed already after the 1st-L/D cycle (Supplementary Figs. S10(a–c)); however, stress relaxation at the flexible film-substrate interface prevents subsequent microcrack widening or propagation. Here, free surfaces (due to microcrack widening during the 1st-L/D cycle) and interfaces play an important role that leads to a much higher stretchability of the Pd thin film during the cycling process. This microstructural stabilization mechanism implicates freedom to expand/contract during H loading/deloading and stress relaxation along the crack spacing. Therefore, one can expect that substrate constrain disappears in the metal thin film without debonding when clamped on a polymer substrate.

Texture analysis: quantification of weak and broad fiber texture

For fiber texture that is not well developed (weak fiber texture), a method has been presented to quantify the volume fraction of the material associated with the texture and random component [62]. This method involves two steps to determine texture volume fraction from ψ -tilt measurements, which includes the entire reflection (2 θ scans) (Supplementary Fig. S9). From the 2 θ scans, the measured (integrated) intensity, $I_{\text{net}}(\psi)$, after a linear background fitting was obtained using the Bruker – EVA software [49]. $I_{\text{net}}(\psi)$ was corrected for thin layer and instrumental intensity loss to obtain the corrected (integrated) intensity, $I_{\text{corr}}(\psi)$ [51]. In the first step, the spread of the texture components is defined by applying Gaussian fitting to the $I_{\text{corr}}(\psi)$ (Supplementary Fig. S11). The occurrence of a texture component, defined as the density of poles, $n(\psi)$, is proportional to the $I_{\text{corr}}(\psi)$. The texture components from the separated intensity maxima (pole density) as a function of ψ are represented employing the pole density plots (PDP) as shown in Fig. 5. The PDP is principally similar to fiber texture plot (FTP), with a cut in a crystallographic direction from the center ($\psi = 0^\circ$) to the outer edge of the pole figure ($\psi = 75^\circ$). The experimental results for the {111} and {200} reflections of Pd thin film in Fig. 5 indicate

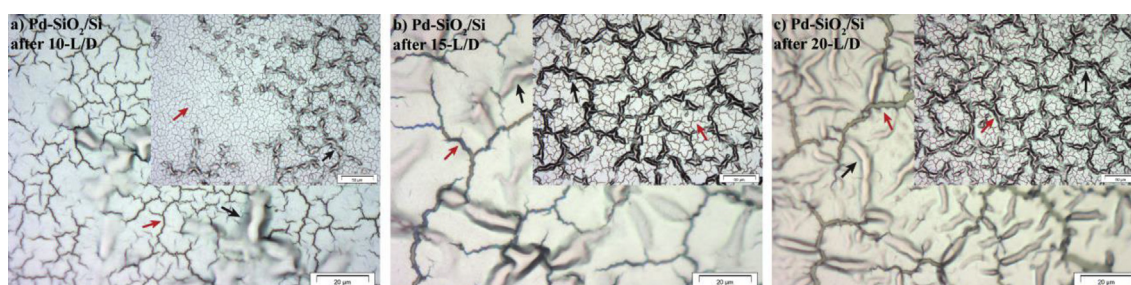


Fig. 4 – Optical microscopy (OM) micrographs with low (50 μm) and high magnification (20 μm) illustrating the formation of the blister network in hydrogen cycled Pd-SiO₂/Si thin film after: (a) 10-L/D cycles, (b) 15-L/D cycles, and (c) 20-L/D cycles. The red arrows indicate hydrogen-induced microcracks and the black arrows indicate delaminated-buckles or blisters in Pd film after loading/deloading cycles. Note that the micrographs were taken from three different samples. (For interpretation of the references to colour in this figure legend, the reader is referred to the Web version of this article.)

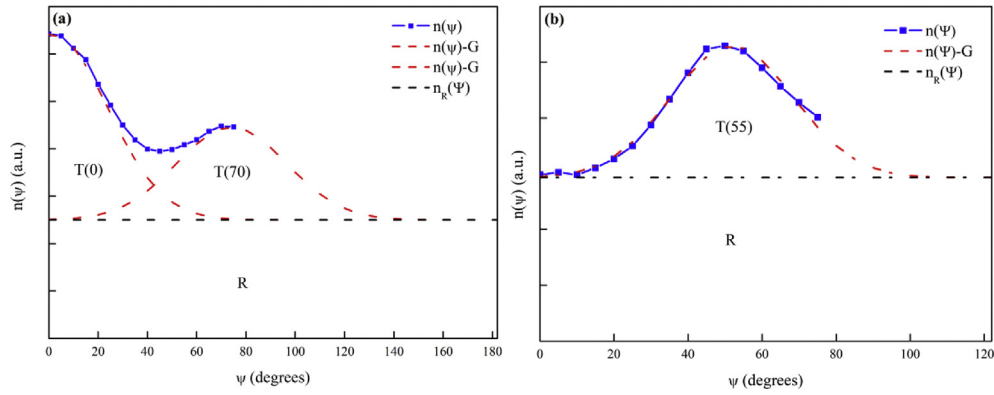


Fig. 5 – Pole density plot (PDP). Density of {111} poles, $n(\psi)$, versus specimen tilting angle ψ for a Pd thin film (Pd-SiO₂/Si) with weak fiber texture: (a) {111}-PDP displaying $\langle 111 \rangle$ fiber texture maxima at $\psi = 0^\circ$ and 70° and (b) {200}-PDP displaying a $\langle 111 \rangle$ fiber texture maxima at $\psi = 55^\circ$.

that the orientation distribution of crystals in the layer is composed of two components: (i) $\langle 111 \rangle$ fiber texture and (ii) a randomly orientated fraction. The breadth of the maximum at $\psi = 0^\circ$ in the {111}-PDP (Fig. 5(a)) is a parameter which is indicative for the “sharpness” of the texture, i.e., spread in the orientation distribution, which amounts to $35\text{--}40^\circ$ in the represented case of the weak fiber texture in Pd thin films.

In the second step, texture components are calculated from the separate intensity maxima in the pole number plot (PNP), represented in Fig. 6. To calculate the total number of poles, i.e., the volume fraction of material associated with the respective texture components, we assumed that the film tilting angle ψ is varied stepwise with an increment $\Delta\psi$. The element of area, $\Delta A(\psi)$, on the surface of the reference hemisphere of the unit radius with the equatorial plane coinciding with the specimen surface is, $\Delta A(\psi) = 2\pi[\cos(\psi - \Delta\psi/2) - \cos(\psi + \Delta\psi/2)]$. The total number of {hkl} poles, $\Delta N(\psi)$, intersecting this area is,

$$\Delta N(\psi) = n(\psi) * \Delta N(\psi) \quad (4)$$

For the Pd thin film, $\Delta N(\psi)$ as derived from $n(\psi)$ (i.e., $I_{\text{corr}}(\psi)$) of {111} and {200} reflections (Fig. 5) are plotted against specimen tilting angle ψ in Fig. 6. The volume fractions of crystallites associated with the respective texture

components can be calculated from the areas T (texture) and R (random) in Fig. 6. First, the random component is considered. The number of poles in an element of an area associated with the random component varies with ψ according to Eq. (4) with a constant value for $n(\psi)\text{-G} = n_R(\psi)$. This constant value is chosen such that the curve for $\Delta N_R(\psi)$ is tangent to the curve for $\Delta N(\psi)\text{-G}$, as shown in Fig. 6. In pole density plots, the Gaussian fitting for the curve $n(\psi)\text{-G}$ was extrapolated beyond the measured $n(\psi)$, i.e., $\psi = 75^\circ$ up to a point, where, $n(\psi)\text{-G} = n_R(\psi)$ (Fig. 5). Due to the presence of minor texture components (Pd- $\langle 311 \rangle$ and $\langle 200 \rangle$, Supplementary Fig. S12(b)) that interfere with pole area of major $\langle 111 \rangle$ -texture component in {111}-PDP, texture quantification for Pd thin film was performed using {200}-PDP. For a $\langle 111 \rangle$ fiber texture, maxima in {200} pole plot occur at $\psi \approx 55^\circ$ (T55), with a $\langle 111 \rangle$ pole multiplicity of 3 (3T55). Taking into account the multiplicity of poles, the volume fraction of crystallite, $f_{\langle 111 \rangle}$, associated with the $\langle 111 \rangle$ texture, was calculated exclusively from the maxima T(55) in Fig. 6(b) from {200} pole number plot:

$$f_{\langle 111 \rangle} = \frac{T(55)}{R + T(55)} = \frac{\sum_{i=1}^{m55} [\Delta N(\psi) - \Delta N_R(\psi)]}{\sum_{i=1}^N \Delta N_R(\psi) + \sum_{i=1}^{m55} [\Delta N(\psi) - \Delta N_R(\psi)]} \quad (5)$$

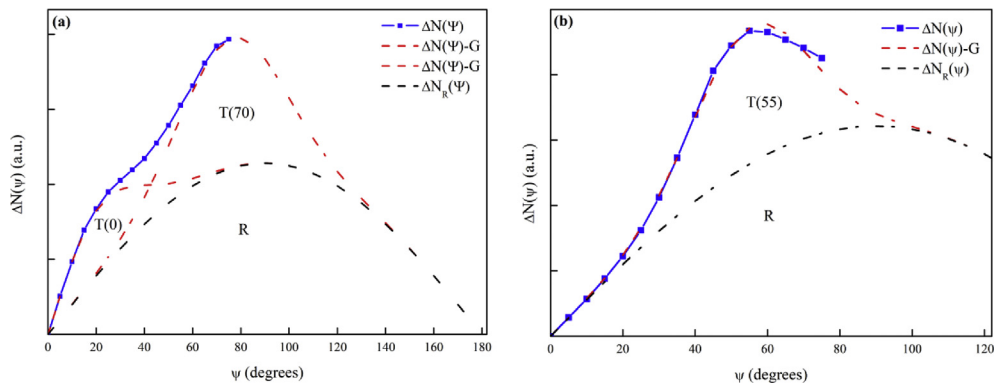


Fig. 6 – Pole number plot (PNP). Number of poles, $\Delta N(\psi)$, in: (a) Pd-{111} and (b) Pd-{200} reflections generated from PDP in Fig. 5. The area T(0) and T(70) in {111}-PNP and area T(55) in {200}-PNP is associated with the $\langle 111 \rangle$ fiber texture, whereas the area R is associated with the randomly oriented crystallites.

where i is the number of the steps in the extrapolated ψ step-scan, and the summation represents the numerical integration of the fitted experimental data over the areas T(55) and R in Fig. 6(b). This extrapolation and integration method is suitable for simple texture quantification of a thin film with weak fiber texture. The method was first successfully established for strong fiber textured Pd thin films for which the overlapped major and minor texture components can be easily separated and calculated (Supplementary Fig. S12).

Texture results for Pd thin films

In Table 2 are listed the volume fractions of (111)-fiber texture, $f_{\langle 111 \rangle}$, and the random (R) component calculated from the {200}-PDP. Quantification of texture component fractions simplifies tracking the texture evolution with H-cycling in Pd thin films. Sharpening of (111)-fiber texture is observed for all Pd thin films studied for hydrogen cycling on two different diffractometers. Likewise, Harumoto et al. [63] have shown for a 48 nm Pd thin film, a change in the grain structure during the cyclic in-plane $\alpha - \beta$ grain boundary motion resulting in in-plane grain growth, lattice defect removal, and (111) texture increase. The Pd thin film is subjected to repeated deformation both during the loading and deloading cycle. This cyclic deformation results in irreversible texture changes. Pivak et al. [31] and Germaud et al. [64], reported film structure evolution in terms of an enhancement of the (111) texture and an increase in crystal size resulting from hydrogen loading and deloading. We found that already after the first H-loading enhancement of the (111) texture is observed as listed in Table 2(b). Furthermore, the volume fraction $f_{\langle 111 \rangle}$ increased both after the hydrogen loading and deloading cycles, indicating the film's structural evolution. This increase in fiber texture can also be correlated to the morphology evolution observed in Section Texture analysis: Quantification of weak and broad fiber texture. Figs. 2 and 3 show hydrogen cycled Pd thin films surface with higher packing density as compared to the as-deposited state, which has low-density open morphology. In our previous works [43,44], we have shown that closed morphology leads to a strong and sharp fiber texture, and

open morphology leads to a weak and broad fiber texture. This kind of morphology and texture evolution influence both the hydrogen uptake response and mode of deformation in the Pd thin film during hydrogen cycling.

Stress analysis

The two methods of tilting the specimen, ω -tilt and ψ -tilt, used for in-situ diffraction stress analysis, are compared in this section.

ω -tilt stress: $\sin^2\psi$ method

Due to the low intensity, asymmetry and poor profile shape of the measured peaks during ω -tilt (Supplementary Fig. S3), it was challenging to determine peak positions with sufficient accuracy and precision. Lattice spacings were evaluated by fitting with the Centered Center of Gravity method using threshold intensity above 40% of the maximum intensity (Supplementary Fig. S13&14). This method is most suitable to find peak positions for asymmetric peaks but cannot distinguish overlapping peaks. Therefore, peak half maxima were used for iteration to avoid overlapping regions between Pd-{331} and {420} peaks. Absorption/transparency correction, background subtraction, LP correction, and $K\alpha_2$ -stripping, as intensity corrections onto the measured scans, were also applied. By fitting the Pd- {331} and {420} diffraction peaks, the central peak positions were obtained for all ψ values. The lattice spacing, d_{ψ} , was calculated using the conventional $\sin^2\psi$ -method [65] and plotted as a function of $\sin^2\psi$ to deduce in-plane stress, $\langle \sigma_{11} \rangle$ in Pd films, from the slope of $d_{(hkl)}$ versus $\sin^2\psi$ for Pd-{331} reflection (Supplementary Fig. S13&14). Hill's weighted average grain-interaction model [65] was applied to calculate the {hkl} dependent X-ray elastic constants for the Pd film reflections. The X-ray elastic constants S_1^{hkl} and $\frac{1}{2}S_2^{hkl}$ values, used for the Pd {331} and {420} reflections, are listed in Table 3. ω -tilt stress measurements were corrected by subtracting ghost stress using a Pd stress-free powder.

Table 2 – Volume fractions of (111)-fiber texture ($f_{\langle 111 \rangle}$) and random component (R) calculated from {200}-PDP in Fig. 6(b). Texture quantification performed on hydrogen cycling experiments was conducted on: (a) D5005 system and (b) PSI-XRD system.

(a) {200}-PDP	Pd-SiO ₂ /Si		Pd-Ti-SiO ₂ /Si		Pd-PI-SiO ₂ /Si	
	Volume fraction		Volume fraction		Volume fraction	
	$f_{\langle 111 \rangle}$	Random	$f_{\langle 111 \rangle}$	Random	$f_{\langle 111 \rangle}$	Random
as-dept. (Pd)	0.25	0.75	0.25	0.75	0.23	0.77
20-L/D (Pd)	0.32	0.68	0.34	0.66	0.30	0.70
(b) {200}-PDP	Pd-Ti-SiO ₂ /Si		Pd-PI-SiO ₂ /Si			
	Volume fraction		Volume fraction			
	$f_{\langle 111 \rangle}$	Random	$f_{\langle 111 \rangle}$	Random		
as-dept. (Pd)	0.32	0.68	0.32	0.68		
1st-L (PdH _{0.66})	0.35	0.65	0.39	0.61		
1-L/D (Pd)	0.39	0.61	0.42	0.58		
20th-L (PdH _{0.66})	0.43	0.57	0.51	0.49		
20-L/D (Pd)	0.46	0.54	0.47	0.53		

Table 3 – X-ray elastic constants for grain-interaction models derived from X'Pert Stress program, using Pd single-crystal elastic constants taken from Ref. [66].

Pd reflections {hkl}	Pd		PdH _{0.66}	
	S_1^{hkl} (TPa ⁻¹)	$\frac{1}{2}S_1^{hkl}$ (TPa ⁻¹)	S_1^{hkl} (TPa ⁻¹)	$\frac{1}{2}S_1^{hkl}$ (TPa ⁻¹)
{111}	-2.16	8.24	-2.38	9.05
{200}	-4.28	14.60	-4.14	14.33
{311}	-3.28	11.60	-3.31	11.84
{331}	-2.54	9.36	-2.69	9.99
{420}	-3.25	11.54	-3.30	11.79

ψ -tilt stress: combining crystallite group method and $\sin^2\psi$ method

In addition to crystallographic texture, the sputter-deposited columnar grain structure is responsible for macroscopic anisotropy in thin films [67]. Therefore, we present an easy approach to estimate stress in Pd thin films by combining the crystallite group method (CGM) [68,69] and the $\sin^2\psi$ method [65]. All individual grains of one group are considered as one single crystal, i.e., possible grain interactions due to different surroundings are neglected. We used all planes parallel to the film surface (in our case, the Pd-{111} oriented grains parallel to the surface) picked from 2 θ scans of Pd- {111}, {200} and {311} reflections (Supplementary Fig. S9). The measured ψ -tilted 0-2 θ scans used for texture quantification were also employed for diffraction stress analysis.

The fiber texture plots (FTP) were used to locate <111> pole positions. The expected <111> pole maxima at $\psi = 0^\circ$ and 70.5° in the {111}-FTP, at $\psi = 54.7^\circ$ in the {200}-FTP, and at $\psi = 29.5^\circ$ and 58.5° in the {311}-FTP were considered for the crystallites with {111} planes parallel to the film surface. The measured peak position at selected ψ -tilt angles corresponding to {111}-oriented grains were used to obtain d-spacing (d_ψ^{hkl}). In the case of strongly textured Pd films, d-spacing for {111}-oriented grains in {hkl} diffraction lines were obtained at the chosen ψ -tilt angles by interpolating data points in d-spacing vs. $\sin^2\psi$ plot (Table 4). For weakly textured Pd thin films, at least three ψ -tilt angles were used at each {111} maxima from {111}-FTP and {200}-FTP (Table 4). Since {311}-FTP did not show maxima for the <111> texture component, the ψ -tilt angles for {111}-oriented grains were based on the expected position, as was observed in strong texture Pd thin film ($\psi = 29.5^\circ$).

CGM requires the conversion of measured d-spacing (of each selected plane) to values of stressed lattice constant (a_ψ^{hkl}) for the cubic system: $a_\psi^{hkl} = d_\psi^{hkl}\sqrt{h^2 + k^2 + l^2}$. The experimentally determined lattice strain ϵ_ψ^{meas} was calculated using the

measured peak position ($2\theta_\psi^{hkl}$), the knowledge of the strain-free lattice constant (a_0^{hkl}) and using Pd lattice constant (a_{ref}) literature value; 3.890 Å, by

$$\epsilon_\psi^{meas} = \left(d_\psi^{hkl} \sqrt{h^2 + k^2 + l^2} - a_0 \right) / a_{ref} = \left(a_\psi^{hkl} - a_0 \right) / a_{ref} \quad (6)$$

For the case of macroscopically elastically anisotropic specimens, the so-called diffraction X-ray elastic constants S_1^{hkl} and $\frac{1}{2}S_2^{hkl}$ relate lattice strain ϵ_ψ^{cal} to the components of stress tensor $\langle \sigma^s \rangle$. For cubic, {111} fiber-textured Pd films the stress state is rotationally symmetric (i.e. $\langle \sigma_{11} \rangle = \langle \sigma_{22} \rangle \equiv \langle \sigma_{11} \rangle$) and ϵ_ψ^{cal} can be obtained from Ref. [70]:

$$\epsilon_\psi^{cal} = \left(2S_1^{hkl} + \frac{1}{2}S_2^{hkl} \sin^2\psi \right) \sigma_{\parallel} \quad (7)$$

We used Hill's weighted average grain-interaction model to estimate the calculated strain. The unknown components of the mechanical stress were evaluated by fitting the calculated strain ϵ_ψ^{cal} (Eq. (7)) to the measured strain ϵ_ψ^{meas} (Eq. (6)) by the use of a least-squares minimization function:

$$\chi^2 = \sum_{i=1}^N \left(\epsilon_i^{cal}(\sigma_{\parallel}, hkl, \psi) - \epsilon_i^{meas}(hkl, \psi) \right)^2 \quad (8)$$

The error related to the measurement of absolute peak positions and imprecise knowledge of strain-free lattice constant can be circumvented if appropriate parameters are included in the fitting of Eq. (8) (Supplementary Fig. S15) [70]. Thus, the strain-free lattice constants (a_0^{hkl}) have been considered as an additional fit parameter along with stress (σ_{11}) (Supplementary Table S1).

Stress results for Pd thin films

The results of stress analysis, measured during hydrogen loading and deloading cycles, are plotted in Fig. 7. The stress values derived by applying the CGM for the {111} crystallite group are shown for Pd on Ti and Pd on PI films as a function of the loading/deloading cycles in Fig. 7(b), while in Fig. 7(a) stress values obtained from the conventional $\sin^2\psi$ method are plotted. Tensile and compressive stresses measured on two different diffractometers and with two different analysis methods give similar trends for stress evolution in hydrogen cycled Pd thin films.

Before the hydrogen gas introduction, the as-deposited Pd thin films are under the influence of in-plane tensile stress, indicating residual stress attributed to sputtering-deposition conditions [44]. The hydrogen loading results in both lattice expansion and a large in-plane compressive stress. The

Table 4 – {hkl} reflections and corresponding ψ -tilt angles, considered for the diffraction stress analysis of the {111}-fiber textured Pd thin films employing a combination of crystallite group method (CGM) and $\sin^2\psi$ method.

Hkl	Strong fiber texture	Weak fiber texture
	ψ ($^\circ$)	ψ ($^\circ$)
{111}	0, 70.5	0, 10, 20, 60, 70 and 75
{200}	54.7	40, 50, 60
{311}	29.5 and 58.5	30

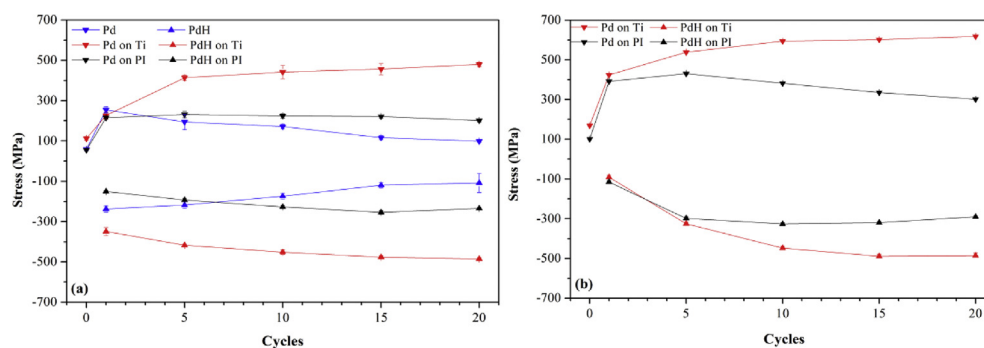


Fig. 7 – In-situ stress vs. 20 H-L/D cycling plots (a) On D5005 system omega-stress analysis for Pd-SiO₂/Si, Pd-Ti-SiO₂/Si, and Pd-PI-SiO₂/Si films and (b) on PSI-XRD system psi-tilt {111}-grain stress analysis for Pd-Ti-SiO₂/Si, and Pd-PI-SiO₂/Si films.

maximum compressive stress during loading cycles was found for Pd-Ti-SiO₂/Si film (max. up to -490 MPa). The large in-plane compressive stress corresponds to the occurrence of the substrate clamping effect, which suppresses the in-plane lattice expansion. This suppression causes a delay in H-up-take in Pd on Ti film along with incomplete $\alpha \rightarrow \beta$ phase transformation as the number of cycles increase (a fraction of a-phase was not transformed) (Supplementary Fig. S6(b)). This is in agreement with a previous observation that a Ti intermediate layer slows down the kinetics of hydrogen absorption/desorption significantly [43]. For Pd-PI-SiO₂/Si film, we see a gradual increase in compressive stress with cycling, but the magnitude is almost half the stress value for Pd on Ti film. The Pd-SiO₂/Si film (without an intermediate layer) shows a decrease in compressive stress with subsequent cycling (Fig. 7(a)). This decrease in stress is correlated to weak cohesion between the Pd film and the substrate, due to which the film is able to provide a free surface by microcrack widening and by film debonding from the substrate (Figs. 3 and 4). In nanocrystalline metal thin films, cracking and delamination contributes to the relaxation of stresses and an additional mechanism of stress relief is that of dislocation motions [71].

During the hydrogen deloading, the large compressive stress in the Pd film is released. After the completion of the first deloading, the stress in all Pd thin films does not return to the initial value (as-deposited) but instead exhibits a large tensile value (Fig. 7). This also indicates that plastic deformation takes place already during the first hydrogen cycle. Note that a large increase in tensile stress is observed between as-deposited state and first deloading for all three Pd films. However, after subsequent cycles, the increase or decrease in tensile stress is small and gradual. Furthermore, for Pd on Ti film, tensile stress keeps increasing with cycling, while for Pd film without an intermediate layer, a decrease is found. For Pd on PI film, tensile stress increases up to 5-L/D cycles, and on further cycling, a gradual decrease is found, similar to Pd-SiO₂/Si film but without compromising its structural integrity. Here, we concluded that for Pd on PI film the large compliance of the polyimide substrate increase crack spacing rearrangements and distance over which stresses are relaxed in the neighborhood of a microcrack.

The overall sequence of hydrogen loading and deloading cycles (20-L/D) shows that the stress evolution behavior is

different for the Pd thin-film systems, and this determines the deformation behavior. In Pd-SiO₂/Si film, the stress relaxation is due to film debonding, while in Pd-Ti-SiO₂/Si film stress builds up due to strong film-substrate bonding. Pd-PI-SiO₂/Si film behavior is in-between the other two films but close to Pd-Ti-SiO₂/Si film. In light of morphology, texture, and stress results, the mechanisms of Pd thin film deformation based on XRD line-broadening analysis are discussed in the next section.

Defects from XRD line-broadening

The presence of crystallographic defects such as dislocations during the microstructural evolution in hydrogen-cycled Pd films was investigated based on the observed change in the integral breadth of diffraction profiles [72]. It is well established that the formation and decomposition of a hydride phase during two-phase transitions results in the generation of a significant dislocation density [47]. Pardoen et al. [46] using time-resolved TEM (HRTEM) demonstrated that the dislocation-mediated mechanism dictates the mechanical stability both during loading (deformation) and deloading (relaxation) in textured nanocrystalline Pd films. Using Bragg coherent diffractive imaging, Ulvestad et al. [23] imaged dislocations nucleated deep in the hydrogen-poor phase during the forward hydriding phase transformation that heal during the reverse transformation in Pd nanoparticles. We used XRD line profiles of the long overview scans from the D5005 system (Section XRD line-broadening: microstructure characterization) for the defect analysis during loading and deloading cycles. The modified Williamson-Hall (mod-WH) method was applied by analyzing the line breadths for all possible types of dislocations [44]. Based on weighted least-square fitted straight lines using the estimated standard deviations in the breadth, it is concluded that randomly oriented pure screw dislocations of the {111}, $a\langle 110 \rangle$ slip system leads to the best fit (mod-WH plot for as-deposited Pd thin films in Supplementary Fig. S16).

In Fig. 8 the values of crystallite size $\langle D \rangle$ and dislocation density ρ (obtained from Mod-WH) plots) are compared to the previous deloading and loading cycles in steps of five. The evolution in $\langle D \rangle$ and ρ is seen during loading when Pd is in the hydrogen-rich phase (β -PdH_{0.66}) and during deloading when

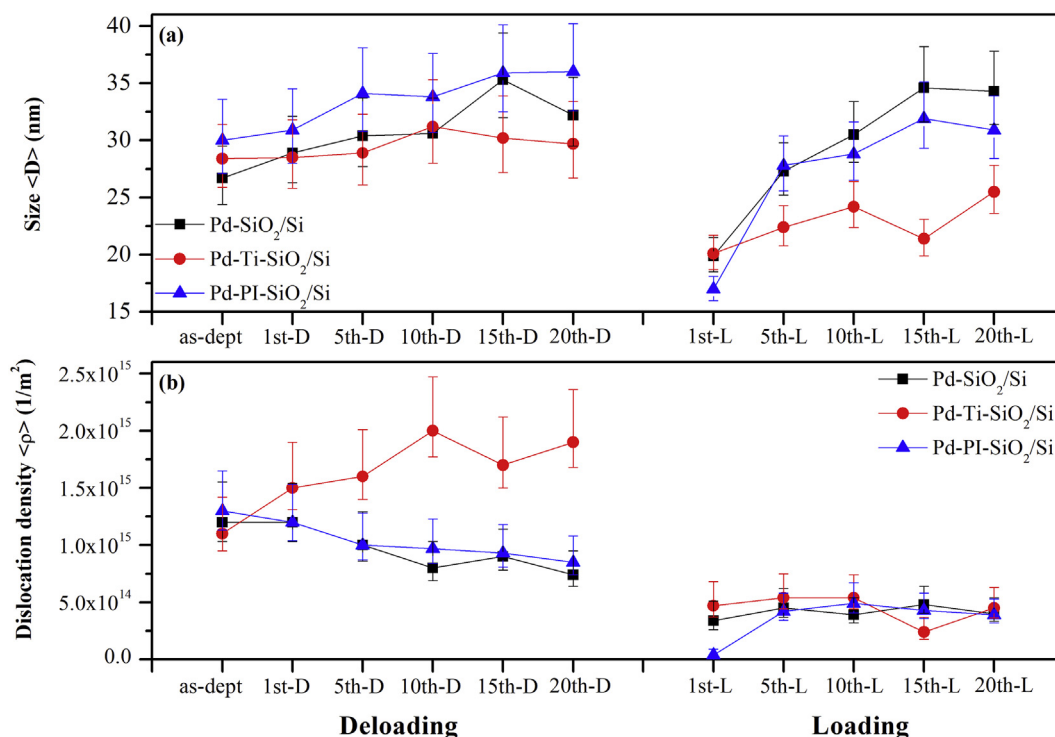


Fig. 8 – Plots with the absolute values of the crystallite size $\langle D \rangle$ (a) and the dislocation density ρ (b) for each of the three Pd thin film systems during 20 hydrogen loading/deloading cycling (20-L/D). On the left side of the plots are Pd films in the metallic phase (Pd) and on the right side are Pd films in the hydrogen-rich phase (β -PdH_{0.66}).

the film returns to the metallic phase (Pd), as in the as-deposited state. With respect to the as-deposited state, a large decrease in crystallite size is observed after 1st loading for all Pd thin films. This is followed by a gradual increase with subsequent cycling, reaching again to almost as-deposited size. While for deloading a stepwise gradual increase in crystallite size is found for all Pd thin films (Fig. 8(a)). This suggests that, during the α – to – β phase transformation, for loading cycles the crystal size is small (Fig. 9(a)). However, once the transformation is completed (α – to – β and β – to – α), the crystal grows large and includes many lattice defects (Fig. 9(a) and b). During the initial hydrogen loading cycles, the β -phase (PdH_{0.66}) exhibits a smaller crystal size than for the completely transformed state (Pd) (Fig. 8(a)). However, after several cycles, the β -phase size reaches almost the same as that of the completely transformed state.

A decrease in dislocation density for all Pd films was found during loading cycles relative to as-deposited and unloaded conditions. Also, the density of dislocations after loading cycles is nearly the same for all Pd films (Fig. 8(b)). However, dislocation development differs for Pd films during deloading cycles. An increase in dislocation density upon deloading is seen for Pd on Ti film, in contrast to a gradual decrease for Pd on PI film and Pd film without an intermediate layer. The possible reason for the decrease in dislocation density for the Pd-SiO₂/Si film is through the formation of a buckled region that has two free surfaces that allow dislocations to escape (Fig. 4(a–c)). In Pd-PI-SiO₂/Si film, also a dislocation density decrease is observed, although no buckling occurred. Here the

film and flexible intermediate layer interface explain the dislocation density decrease. The dislocations are annihilated at the crystalline-amorphous interface with the polyimide intermediate layer, which acts as a dislocation sink [73]. This suggests that the Pd-PI interface behaves like a free surface with respect to the stability of dislocations.

In Fig. 9, the cyclic behavior of the $\langle D \rangle$ and ρ during loading and deloading cycles is visualized. The general behavior (shapes of the plot) is the same for all three Pd films, which testifies that all Pd films contain similar kinds of defects, that differ only by their concentration. In all likelihood, the dislocations propagate and interact with pre-existing microstructure and also with each other, thus making up the final microstructure of the deformed state. Fig. 9(a) shows a different pattern of $\langle D \rangle$ towards the end (higher cycles) for Pd-SiO₂/Si film that can be explained by buckle formation (Fig. 4). The cyclic evolution of crystallite size, decrease during loading and increase upon deloading confirm that the presence of GB-mediated mechanisms contributes to the relaxation process in columnar grained Pd thin films. Fig. 9(b) shows also that during loading, when compressive stress develops, dislocation densities are reduced, and are strongly retrieved after deloading when the film is again under tensile stress. Thus, the change in residual stress from compressive to tensile increases lattice strain, resulting in high dislocation densities at the end of the loading/deloading cycle. The defect analysis shows the reversible pattern of grain growth and dislocation generation/motion when stresses change between tensile and compressive during hydrogen cycling. The correlation between stress relaxation and change in dislocation

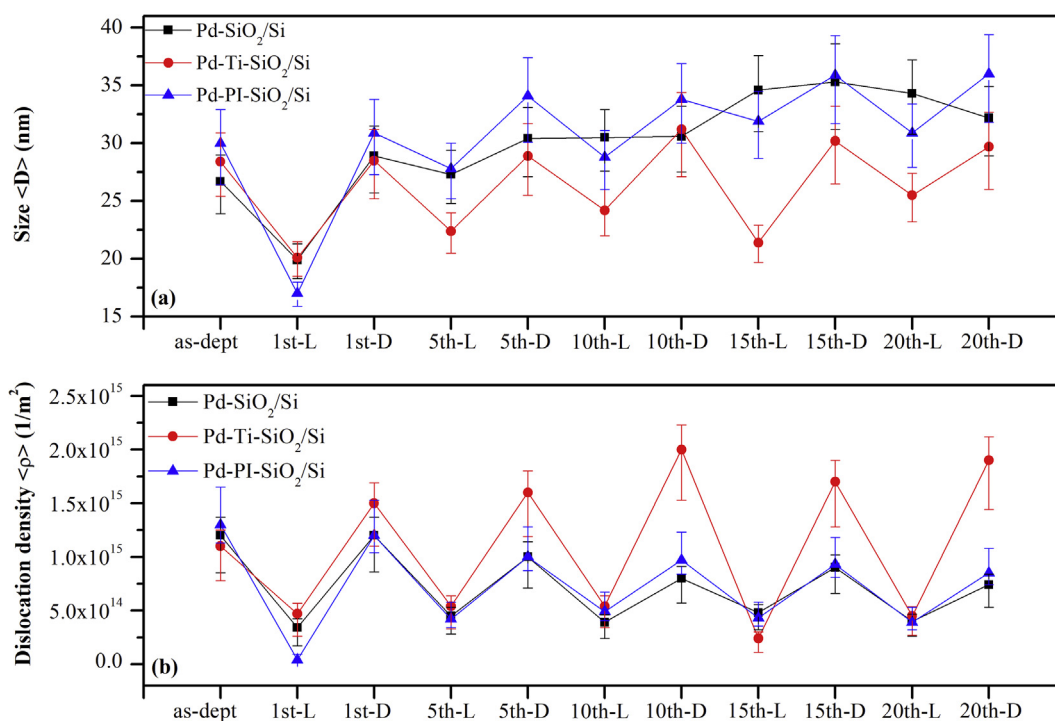


Fig. 9 – The crystallite size $\langle D \rangle$ (a) and the dislocation density ρ (b) plots to show its cyclic behavior during 20 hydrogen loading/deloading cycling (20-L/D). During loading, films are in the hydrogen-rich phase (β -PdH_{0.66}) and during deloading films return to the metallic phase (Pd), as in the as-deposited state.

density is based on the idea that the dislocation decreases by the annihilation of dislocation at sinks (e.g. grain boundaries, microcrack or film-substrate interface). Ulvestad et al. [23] showed that at a certain critical size of Pd nanoparticles, dislocations are generated to relieve the stress. Further, they showed the formation and healing of structural defects in Pd nanoparticles during the $\alpha \leftrightarrow \beta$ phase transformation. A similar kind of stability and mobility of dislocation can be seen in our Pd films during cyclic phase transformations. We conclude that films with an open morphology successfully restrict internal stress from amplifying during hydrogen uptake, and thus no noticeable structural deformation occurs for films with a stable film-substrate interface.

Similar to Pd nanoparticles, Pd thin films follow similar behavior, except for the stress relaxation mode at critical stress values, which depends on film-substrate stability. The dislocation-based relaxation mechanism depends both on the generation of new dislocations and the propagation of the existing dislocations. The strengthening of thin films in terms of threading dislocations is possible when the increase in dislocation energy equals the film strain energy reduction, leading to the Nix-Freund relation [74,75]. From a dislocation distribution point of view, on a strongly adhering substrate (Ti-SiO₂/Si), dislocation repulsions are higher at the interface than for film attached on a flexible substrate (PI-SiO₂/Si) or on to a substrate with poor adherence (SiO₂/Si). The possibility of concurrent microcracking and buckling allows delamination to occur in Pd film without the adhesive intermediate layer, while a flexible PI intermediate layer allows Pd film to “breathe” during hydrogen cycling, along with providing enhanced adhesive support to the film on the substrate.

Conclusion

In-situ X-ray diffraction (XRD) study of hydrogen cycling on Pd thin films has been conducted to deduce the intermediate layer's (substrate types) influence on the morphology, preferred orientation (texture), and state of stress as a function of the film substrate types and hydrogen cycling. We present a simple method to estimate texture-components volume fractions in weak fiber texture Pd thin films. This method can be immediately implemented to study texture evolution during hydrogen cycling. It was found that the hydrogen cycling results in an increase in {111}-fiber texture. The diffraction stress analysis was performed by combining the $\sin^2\psi$ method and the crystallite group method (CGM) to enable the determination of stress values for macroscopically elastically anisotropic Pd thin films. The stress results show that the stress evolution during cycling is different for all three Pd thin film systems, and this determines the deformation behavior. These findings are further supported by transmission and scanning electron microscopy (TEM and SEM) investigations for morphological changes and through diffraction line-broadening analysis to understand the deformation mechanism. The plastic deformation occurs both during loading and deloading in Pd film and leads to changes in the dislocation density in the final microstructure of the deformed state. Scanning electron and optical micrographs show that debonding plays a critical role in Pd-SiO₂/Si film failure mechanism. By using a flexible and adhesive intermediate layer – like with polyimide one can enhance the stability of the Pd thin films.

Declaration of competing interest

The authors declare that they have no known competing financial interests or personal relationships that could have appeared to influence the work reported in this paper.

Acknowledgments

This work was financially supported by the Delft University of Technology. We would like to acknowledge Dr. Frans D. Tichelaar at the HREM group at the Kavli Institute of Nano-Science, Delft University of Technology for the TEM cross-section images. We thank Prof dr. ir. J. Sietsma (Department of Materials Science and Engineering, Delft University of Technology) for his feedback on the manuscript.

Appendix A. Supplementary data

Supplementary data to this article can be found online at <https://doi.org/10.1016/j.ijhydene.2022.01.233>.

REFERENCES

- [1] Barreto L, Makihira A, Riahi K. The hydrogen economy in the 21st century: a sustainable development scenario. *Int J Hydrogen Energy* 2003;28:267–84. [https://doi.org/10.1016/S0360-3199\(02\)00074-5](https://doi.org/10.1016/S0360-3199(02)00074-5).
- [2] Ball M, Weeda M. The hydrogen economy—vision or reality? *Int J Hydrogen Energy* 2015;40:7903–19. <https://doi.org/10.1016/j.ijhydene.2015.04.032>.
- [3] Abe J, Popoola A, Ajenifuja E, Popoola O. Hydrogen energy, economy and storage: review and recommendation. *Int J Hydrogen Energy* 2019;44:15072–86. [https://doi.org/10.1016/S1369-7021\(11\)70143-2](https://doi.org/10.1016/S1369-7021(11)70143-2).
- [4] Boudart M, Hwang H. Solubility of hydrogen in small particles of palladium. *J Catal* 1975;39:44–52. [https://doi.org/10.1016/0021-9517\(75\)90280-8](https://doi.org/10.1016/0021-9517(75)90280-8).
- [5] Flanagan TB, Oates W. The palladium-hydrogen system. *Annu Rev Mater Sci* 1991;21:269–304. <https://doi.org/10.1146/annurev.ms.21.080191.001413>.
- [6] Jewell LL, Davis BH. Review of absorption and adsorption in the hydrogen–palladium system. *Appl Catal Gen* 2006;310:1–15. <https://doi.org/10.1016/j.apcata.2006.05.012>.
- [7] Griessen R, Strohhfeldt N, Giessen H. Thermodynamics of the hybrid interaction of hydrogen with palladium nanoparticles. *Nat Mater* 2016;15:311–7. <https://doi.org/10.1038/nmat4480>.
- [8] Harumoto T, Nakamura Y, Shi J. Correlation among hydrogenation, magnetoelastic coupling, magnetic anisotropy, and magnetoresistance in magnetostrictive, hydrogen-absorbing palladium-cobalt alloy films for hydrogen sensing. *Int J Hydrogen Energy* 2021;46:30204–15. <https://doi.org/10.1016/j.ijhydene.2021.06.163>.
- [9] Sousanis A, Biskos G. Thin film and nanostructured Pd-based materials for optical H₂ sensors: a review. *Nanomaterials* 2021;11:3100. <https://doi.org/10.3390/nano11113100>.
- [10] Westerwaal R, Den Besten C, Slaman M, Dam B, Nanu D, Böttger A, et al. High throughput screening of Pd-alloys for H₂ separation membranes studied by hydrogenography and CVM. *Int J Hydrogen Energy* 2011;36:1074–82. <https://doi.org/10.1016/j.ijhydene.2010.10.014>.
- [11] Nayebossadri S, Speight JD, Book D. Hydrogen separation from blended natural gas and hydrogen by Pd-based membranes. *Int J Hydrogen Energy* 2019;44:29092–9. <https://doi.org/10.1016/j.ijhydene.2019.03.044>.
- [12] Narehood D, Kishore S, Goto H, Adair J, Nelson J, Gutierrez H, et al. X-ray diffraction and H-storage in ultra-small palladium particles. *Int J Hydrogen Energy* 2009;34:952–60. <https://doi.org/10.1016/j.ijhydene.2008.10.080>.
- [13] Li G, Kobayashi H, Taylor JM, Ikeda R, Kubota Y, Kato K, et al. Hydrogen storage in Pd nanocrystals covered with a metal–organic framework. *Nat Mater* 2014;13:802–6. <https://doi.org/10.1038/nmat4030>.
- [14] Manchester F, San-Martin A, Pitre J. The H-Pd (hydrogen-palladium) system. *J Phase Equil* 1994;15:62–83.
- [15] Conrad H, Ertl G, Latta E. Adsorption of hydrogen on palladium single crystal surfaces. *Surf Sci* 1974;41:435–46. [https://doi.org/10.1016/0039-6028\(74\)90060-0](https://doi.org/10.1016/0039-6028(74)90060-0).
- [16] Schneemann A, White JL, Kang S, Jeong S, Wan LF, Cho ES, et al. Nanostructured metal hydrides for hydrogen storage. *Chem Rev* 2018;118:10775–839. <https://doi.org/10.1021/acs.chemrev.8b00313>.
- [17] Callini E, Aguey-Zinsou K-F, Ahuja R, Ares JR, Bals S, Biliškov N, et al. Nanostructured materials for solid-state hydrogen storage: a review of the achievement of COST Action MP1103. *Int J Hydrogen Energy* 2016;41:14404–28. <https://doi.org/10.1016/j.ijhydene.2016.04.025>.
- [18] Bardhan R, Hedges LO, Pint CL, Javey A, Whitelam S, Urban JJ. Uncovering the intrinsic size dependence of hydriding phase transformations in nanocrystals. *Nat Mater* 2013;12:905–12. <https://doi.org/10.1038/nmat3716>.
- [19] Sengar SK, Mehta B, Kulriya P. Temperature, pressure, and size dependence of Pd-H interaction in size selected Pd-Ag and Pd-Cu alloy nanoparticles: in-situ X-ray diffraction studies. *J Appl Phys* 2014;115:114308. <https://doi.org/10.1063/1.4868903>.
- [20] Eastman J, Thompson L, Kestel B. Narrowing of the palladium-hydrogen miscibility gap in nanocrystalline palladium. *Phys Rev B* 1993;48:84. <https://doi.org/10.1103/PhysRevB.48.84>.
- [21] Hakamada M, Nakano H, Furukawa T, Takahashi M, Mabuchi M. Hydrogen storage properties of nanoporous palladium fabricated by dealloying. *J Phys Chem C* 2010;114:868–73. <https://doi.org/10.1021/jp909479m>.
- [22] Narayan TC, Hayee F, Baldi A, Koh AL, Sinclair R, Dionne JA. Direct visualization of hydrogen absorption dynamics in individual palladium nanoparticles. *Nat Commun* 2017;8:14020. <https://doi.org/10.1038/ncomms14020>.
- [23] Ulvestad A, Yau A. The self-healing of defects induced by the hydriding phase transformation in palladium nanoparticles. *Nat Commun* 2017;8:1–6. <https://doi.org/10.1038/s41467-017-01548-7>.
- [24] Pundt A, Kirchheim R. Hydrogen in metals: microstructural aspects. *Annu Rev Mater Res* 2006;36:555–608. <https://doi.org/10.1146/annurev.matsci.36.090804.094451>.
- [25] Vlček M, Lukáč F, Vlach M, Wagner S, Uchida H, Baehtz C, et al. Influence of microstructure and mechanical stress on behavior of hydrogen in 500nm Pd films. *J Alloys Compd* 2015;645. <https://doi.org/10.1016/j.jallcom.2014.12.086>. S446–S9.
- [26] Okolo B, Lamparter P, Welzel U, Wagner T, Mittemeijer E. The effect of deposition parameters and substrate surface condition on texture, morphology and stress in magnetron-sputter-deposited Cu thin films. *Thin Solid Films* 2005;474:50–63. <https://doi.org/10.1016/j.tsf.2004.08.006>.

- [27] Thompson CV. Structure evolution during processing of polycrystalline films. *Annu Rev Mater Sci* 2000;30:159–90. <https://doi.org/10.1146/annurev.matsci.30.1.159>.
- [28] Cortie M. Calculation of texture volume fractions by integration and Gaussian fitting. *Textures Microstruct* 1997;29:155–84. <https://doi.org/10.1155/TSM.29.155>.
- [29] Wagner S, Pundt A. Combined impact of microstructure and mechanical stress on the electrical resistivity of PdHc thin films. *Acta Mater* 2011;59:1862–70. <https://doi.org/10.1016/j.actamat.2010.11.052>.
- [30] Delmelle R, Amin-Ahmadi B, Sinnaeve M, Idrissi H, Pardoen T, Schryvers D, et al. Effect of structural defects on the hydriding kinetics of nanocrystalline Pd thin films. *Int J Hydrogen Energy* 2015;40:7335–47. <https://doi.org/10.1016/j.ijhydene.2015.04.017>.
- [31] Pivak Y, Schreuders H, Slaman M, Griessen R, Dam B. Thermodynamics, stress release and hysteresis behavior in highly adhesive Pd–H films. *Int J Hydrogen Energy* 2011;36:4056–67. <https://doi.org/10.1016/j.ijhydene.2010.12.063>.
- [32] Vlček M, Lukáč F, Vlach M, Procházka I, Wagner S, Uchida H, et al. Hydrogen-induced buckling of Pd films deposited on various substrates. *Defect Diffusion Forum* 2015;365:55–62. <https://doi.org/10.4028/www.scientific.net/DDF.365.55>.
- [33] Li T, Suo Z. Ductility of thin metal films on polymer substrates modulated by interfacial adhesion. *Int J Solid Struct* 2007;44:1696–705. <https://doi.org/10.1016/j.ijsolstr.2006.07.022>.
- [34] Abadias G, Chason E, Keckes J, Sebastiani M, Thompson GB, Barthel E, et al. Stress in thin films and coatings: current status, challenges, and prospects. *J Vac Sci Technol* 2018;36:20801. <https://doi.org/10.1116/1.5011790>.
- [35] Welzel U, Mittemeijer EJ. Diffraction stress analysis of macroscopically elastically anisotropic specimens: on the concepts of diffraction elastic constants and stress factors. *J Appl Phys* 2003;93:9001–11. <https://doi.org/10.1063/1.1569662>.
- [36] Van Leeuwen M, Kamminga J-D, Mittemeijer E. Diffraction stress analysis of thin films: modeling and experimental evaluation of elastic constants and grain interaction. *J Appl Phys* 1999;86:1904–14. <https://doi.org/10.1063/1.370986>.
- [37] Welzel U, Mittemeijer EJ. Applicability of the crystallite group method to fibre textured specimens. *Mater Sci* 2004;131–6. <https://doi.org/10.4028/www.scientific.net/MSF.443-444.131>.
- [38] Liu Y, Wang C, Tan H. Growth from buckling to buckling-driven delamination in a film/substrate system. *Compos Struct* 2017;174:292–300. <https://doi.org/10.1016/j.compstruct.2017.04.062>.
- [39] Xia ZC, Hutchinson JW. Crack patterns in thin films. *J Mech Phys Solid* 2000;48:1107–31. [https://doi.org/10.1016/S0022-5096\(99\)00081-2](https://doi.org/10.1016/S0022-5096(99)00081-2).
- [40] Liu D, Pons DJ. Crack propagation mechanisms for creep fatigue: a consolidated explanation of fundamental behaviours from initiation to failure. *Metals* 2018;8:623. <https://doi.org/10.3390/met8080623>.
- [41] Lee J, Shim W, Lee E, Noh JS, Lee W. Highly mobile palladium thin films on an elastomeric substrate: nanogap-based hydrogen gas sensors. *Angew Chem Int Ed* 2011;50:5301–5. <https://doi.org/10.1002/anie.201100054>.
- [42] Lu N, Wang X, Suo Z, Vlassak J. Metal films on polymer substrates stretched beyond 50%. *Appl Phys Lett* 2007;91:221909. <https://doi.org/10.1063/1.2817234>.
- [43] Verma N, Krishnamurthy G, Tichelaar FD, Böttger AJ. Controlling morphology and texture of sputter-deposited Pd films by tuning the surface topography of the (Ti) adhesive layer. *Surf Coating Technol* 2019;359:24–34. <https://doi.org/10.1016/j.surfcoat.2018.12.053>.
- [44] Verma N, Delhez R, van der Pers NM, Tichelaar FD, Böttger AJ. The role of the substrate on the mechanical and thermal stability of Pd thin films during hydrogen (de) sorption. *Int J Hydrogen Energy* 2020;46:4137–53. <https://doi.org/10.1016/j.ijhydene.2020.10.163>.
- [45] Flanagan TB, Bowerman B, Biehler G. Hysteresis in metal/hydrogen systems. *Scripta Metall* 1980;14:443–7. [https://doi.org/10.1016/0036-9748\(80\)90342-7](https://doi.org/10.1016/0036-9748(80)90342-7).
- [46] Colla MS, Amin-Ahmadi B, Idrissi H, Malet L, Godet S, Raskin JP, et al. Dislocation-mediated relaxation in nanograined columnar palladium films revealed by on-chip time-resolved HRTEM testing. *Nat Commun* 2015;6:5922. <https://doi.org/10.1038/ncomms6922>.
- [47] Amin-Ahmadi B, Connétable D, Fivel M, Tanguy D, Delmelle R, Turner S, et al. Dislocation/hydrogen interaction mechanisms in hydrided nanocrystalline palladium films. *Acta Mater* 2016;111:253–61. <https://doi.org/10.1016/j.actamat.2016.03.054>.
- [48] SRM660a. Lanthanum hexaboride powder line position and line shape standard for powder diffraction. Certificate. Gaithersburg, MD, USA: National Institute of Standards and Technology, US Department of Commerce; 2000. <https://www.nist.gov/srm>.
- [49] DIFFRAC.EVA. Bruker AXS software, karlsruhe, Germany. <https://www.bruker.com/>; 2001.
- [50] Scardi P, Leoni M, Dong Y. Texture determination in highly stressed PVD thin films. *Adv X Ray Anal* 2000;42:492–501.
- [51] Welzel U, Leoni M. Use of polycapillary X-ray lenses in the X-ray diffraction measurement of texture. *J Appl Crystallogr* 2002;35:196–206. <https://doi.org/10.1107/S0021889802000481>.
- [52] PANalytical X'Pert Stress Plus. PANalytical, Almelo, The Netherlands. <https://www.malvernpanalytical.com/>; 2012.
- [53] Scardi P, Leoni M, Delhez R. Line broadening analysis using integral breadth methods: a critical review. *J Appl Crystallogr* 2004;37:381–90. <https://doi.org/10.1107/S0021889804004583>.
- [54] Velterop L, Delhez R, Keijsers THd, Mittemeijer E, Reefman D. X-ray diffraction analysis of stacking and twin faults in fcc metals: a revision and allowance for texture and non-uniform fault probabilities. *J Appl Crystallogr* 2000;33:296–306. <https://doi.org/10.1107/S0021889800000133>.
- [55] Williamson G, Hall W. X-ray line broadening from filed aluminium and wolfram. *Acta Metall* 1953;1:22–31. [https://doi.org/10.1016/0001-6160\(53\)90006-6](https://doi.org/10.1016/0001-6160(53)90006-6).
- [56] Ungár T, Dragomir I, Révész Á, Borbély A. The contrast factors of dislocations in cubic crystals: the dislocation model of strain anisotropy in practice. *J Appl Crystallogr* 1999;32:992–1002. <https://doi.org/10.1107/S0021889899009334>.
- [57] Gubicza J. X-ray line profile analysis in materials science. Hershey, Pennsylvania: Engineering Science Reference; 2014. <http://doi:10.4018/978-1-4666-5852-3>.
- [58] Verma N, Böttger AJ. Stress development and adhesion in hydrogenated nano-columnar Pd and Pd/Ti ultra-thin films. *Adv Mater Res* 2014;996. <https://doi.org/10.4028/www.scientific.net/AMR.996.872>.
- [59] Liu D, Pons D. Crack propagation mechanisms for creep fatigue: a consolidated explanation of fundamental behaviours from initiation to failure. *Metals* 2018;8:623. <https://doi.org/10.3390/met8080623>.
- [60] Shamsutdinov N, Böttger A, Thijsse B. Grain coalescence and its effect on stress and elasticity in nanocrystalline metal films. *Acta Mater* 2007;55:777–84. <https://doi.org/10.1016/j.actamat.2006.07.004>.
- [61] Li T, Huang Z, Xi Z, Lacour SP, Wagner S, Suo Z. Delocalizing strain in a thin metal film on a polymer substrate. *Mech Mater* 2005;37:261–73. <https://doi.org/10.1016/j.mechmat.2004.02.002>.

- [62] Hendriks M. X-ray diffraction study of polycrystalline silicon layers. <http://resolver.tudelft.nl/uuid:b62d5d7f-b6fb-4f73-a880-a3c027d8ef9d>; 1985.
- [63] Harumoto T, Ohnishi Y, Nishio K, Ishiguro T, Shi J, Nakamura Y. In-situ X-ray diffraction study of hydrogen absorption and desorption processes in Pd thin films: hydrogen composition dependent anisotropic expansion and its quantitative description. *AIP Adv* 2017;7:65108. <https://doi.org/10.1063/1.4986214>.
- [64] Gremaud R, Gonzalez-Silveira M, Pivak Y, De Man S, Slaman M, Schreuders H, et al. Hydrogenography of PdHx thin films: influence of H-induced stress relaxation processes. *Acta Mater* 2009;57:1209–19. <https://doi.org/10.1016/j.actamat.2008.11.016>.
- [65] Hauk V. Structural and residual stress analysis by nondestructive methods: evaluation-Application-Assessment. Elsevier; 1997. <https://doi.org/10.1016/B978-0-444-82476-9.X5000-2>.
- [66] Hsu D, Leisure R. Elastic constants of palladium and β -phase palladium hydride between 4 and 300 K. *Phys Rev B* 1979;20:1339–44. <https://doi.org/10.1103/PhysRevB.20.1339>.
- [67] Welzel U, Mittemeijer EJ. Diffraction stress analysis of macroscopically elastically anisotropic specimens: on the concepts of diffraction elastic constants and stress factors. *J Appl Phys* 2003;93:9001. <https://doi.org/10.1063/1.1569662>.
- [68] Gergaud P, Labat S, Thomas O. Limits of validity of the crystallite group method in stress determination of thin film structures. *Thin Solid Films* 1998;319:9–15. [https://doi.org/10.1016/S0040-6090\(97\)01100-0](https://doi.org/10.1016/S0040-6090(97)01100-0).
- [69] Faurie D, Renault P-O, Le Bourhis E, Goudeau P. Study of texture effect on elastic properties of Au thin films by X-ray diffraction and in situ tensile testing. *Acta Mater* 2006;54:4503–13. <https://doi.org/10.1016/j.actamat.2006.05.036>.
- [70] Welzel U, Leoni M, Mittemeijer E. The determination of stresses in thin films; modelling elastic grain interaction. *Phil Mag* 2003;83:603–30. <https://doi.org/10.1080/0141861021000042299>.
- [71] Thouless M. Modeling the development and relaxation of stresses in films. *Annu Rev Mater Sci* 1995;25:69–96.
- [72] Delhez R, De Keijser TH, Mittemeijer E. Determination of crystallite size and lattice distortions through X-ray diffraction line profile analysis. *Fresenius' Z für Anal Chem* 1982;312:1–16. <https://doi.org/10.1007/BF00482725>.
- [73] Legros M, Cabié M, Gianola DS. In situ deformation of thin films on substrates. *Microsc Res Tech* 2009;72:270–83. <https://doi.org/10.1002/jemt.20680>.
- [74] Nix WD. Mechanical properties of thin films. *Metall Trans A* 1989;20:2217–45. <https://doi.org/10.1007/BF02666659>.
- [75] Freund L. The stability of a dislocation threading a strained layer on a substrate. *J Appl Mech* 1987;54:553–7. <https://doi.org/10.1115/1.3173068>.